AIAA JOURNAL
Vol. 30, No. 10, October 1992

Numerical Study of Shock-Wave/Boundary-Layer Interactions in Premixed Combustible Gases

Shaye Yungster*
NASA Lewis Research Center, Cleveland, Ohio 44135

A computational study of shock-wave/boundary-layer interactions involving premixed combustible gases is presented. The analysis is carried out using a new fully implicit, total variation diminishing code that solves the fully coupled Reynolds-averaged Navier-Stokes equations and species continuity equations in an efficient manner. To accelerate the convergence of the basic iterative procedure, the code is combined with vector extrapolation methods. The chemical nonequilibrium processes are simulated by means of a finite-rate chemistry model for hydrogen-air combustion. The investigation is conducted on a ramjet-in-tube projectile accelerator concept known as the "ram accelerator." Results indicate a combustion mechanism in which a shock wave induces combustion in the boundary layer, which then couples with the reflected shock, forming a shock-deflagration wave. At higher Mach numbers, spontaneous combustion in part of the boundary layer is observed, which eventually extends along the entire boundary layer at still higher values of the Mach number.

Introduction

THE interactions that occur when a shock wave impinges on a boundary layer have been extensively studied in the past. A summary of such research can be found, for example, in Refs. 1 and 2 for laminar and turbulent boundary layers. Most of these studies have concentrated on nonreacting airflows. In recent years, the renewed interest in hypersonic air-breathing vehicles and hypervelocity mass launchers has created the need to investigate shock-wave/boundary-layer interactions involving combustible gas mixtures and the resulting combustion processes. This type of interaction is present in such hypersonic propulsion concepts as the supersonic combustion ramjet (scramjet), the oblique detonation wave engine (ODWE), and the ram accelerator. Obtaining a good understanding of this type of interaction is particularly important for the ram accelerator, a ramjet-in-tube concept that is the main subject of the present paper.

The ram accelerator is a hypervelocity mass launcher device in which a shaped projectile can in principle be accelerated efficiently to velocities in excess of 10 km/s by means of detonation waves or other shock-induced combustion modes. This concept, developed at the University of Washington,[3-9] can be scaled for projectile masses ranging from grams to hundreds of kilograms and has the potential for a number of applications, such as hypervelocity impact physics, direct launch to orbit of acceleration insensitive payloads, and hypersonic testing.[9-10] An experimental ram accelerator device, currently operating at the University of Washington, has reached velocities in excess of 2.6 km/s and Mach numbers as high as 8.4.

Although several ram accelerator operation modes have been proposed,[3] the analysis in this paper will be centered on the "oblique detonation" mode shown in Fig. 1. The gasdynamic principles of the oblique detonation ram accelerator are similar to those of the ODWE concept; however, the device is operated in a different manner.

In the oblique detonation ram accelerator (Fig. 1), the centerbody is a projectile fired into a tube filled with a premixed gaseous fuel/oxidizer mixture. There is no propellant onboard the projectile. Ignition of the fuel/oxidizer mixture is achieved by means of a series of shock waves that increase its temperature. When the ignition temperature is reached at a designed location, rapid chemical reactions release energy into the flowing stream. The energy addition will establish either a detonation wave or a shock-deflagration wave, depending primarily on the mixture composition, pressure, and tube size. The combustion process creates a high pressure region over the back of the projectile, producing a thrust force. Since the fuel and oxidizer in the ram accelerator concept are premixed, the difficulties in obtaining rapid and complete mixing encountered by the ODWE (and the conventional scramjet) are circumvented.

The performance of the oblique detonation ram accelerator has been evaluated in the past by using one of the following approaches: 1) simplified one-dimensional flow models (Humphrey,[10] Rom and Kivity,[11] and Yip et al.[12]) or 2) numerical simulations based on inviscid computational fluid dynamics (CFD) methods (Brackett and Bogdanoff[5] and Yungster et al.[6,7]).

The results presented in all of the aforementioned studies have confirmed the potential of the ram accelerator to efficiently accelerate projectiles to velocities in excess of 10 km/s. In these studies, however, the effects of viscosity, heat conduction, and mass diffusion have all been neglected. In the ram accelerator concept these transport processes can become

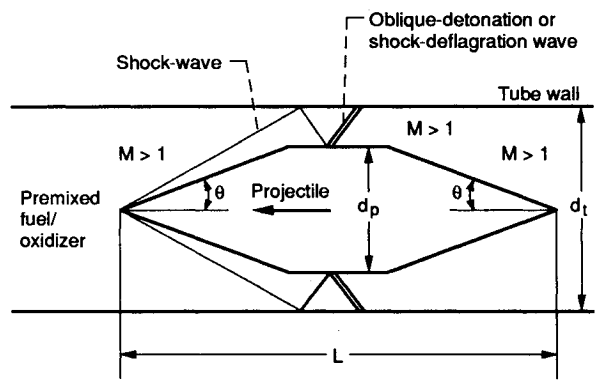

Fig. 1 Schematic of oblique detonation ram accelerator concept (L = 15 cm, d_p = 2.5 cm, d_t = 3.8 cm, θ = 14 deg).

Presented as Paper 91-0413 at the AIAA 29th Aerospace Sciences Meeting, Reno, NV, Jan. 7-10, 1991; received Feb. 21, 1991; revision received April 14, 1992; accepted for publication April 14, 1992.

*Research Associate, Institute for Computational Mechanics in Propulsion. Member AIAA.

very important since a boundary layer consisting of premixed combustible gases will develop on the surface of the projectile. The objective of the present paper is to investigate numerically the combustion processes that can occur in such a boundary layer. These combustion processes can be initiated by either spontaneous ignition due to viscous dissipation or by one of the reflected shock waves.

The approach taken is to seek solutions of the full Reynolds-averaged Navier-Stokes equations, including the reaction kinetics of a seven-species, eight-step hydrogen/oxygen combustion model, using a new CFD code. The code uses an iterative scheme that is based on the LU-SSOR implicit factorization scheme and a second-order symmetric total variation diminishing (TVD) differencing scheme. The iterative scheme can further be combined with vector extrapolation methods to enhance its convergence properties. Extrapolation methods have been used in conjunction with iterative schemes in CFD codes, mostly for the Euler equations. To the author's knowledge, there have not been any applications in reacting flow problems. The extrapolation methods used in the present study are the minimal polynomial extrapolation (MPE) and the reduced rank extrapolation (RRE).

The numerical formulation, iterative scheme, and extrapolation method used in the present work are described in the following sections.

Numerical Formulation

Governing Equations

The Reynolds-averaged Navier-Stokes equations for two-dimensional or axisymmetric flow are considered. For the case of chemically reacting flows, the global continuity equation is replaced by all of the species continuity equations. They can be expressed in the following conservation form for a gas containing n species and in general curvilinear coordinates (ξ, η):

$$\frac{\partial \boldsymbol{Q}}{\partial t} + \frac{\partial (\boldsymbol{F} - \boldsymbol{F}_v)}{\partial \xi} + \frac{\partial (\boldsymbol{G} - \boldsymbol{G}_v)}{\partial \eta} + j(\boldsymbol{H} - \boldsymbol{H}_v) = \boldsymbol{W} \tag{1}$$

where

$$\boldsymbol{Q} = J^{-1}\begin{bmatrix} \rho_1 \\ \rho_2 \\ \vdots \\ \rho_n \\ \rho u \\ \rho v \\ e \end{bmatrix}, \qquad \boldsymbol{F} = J^{-1}\begin{bmatrix} \rho_1 U \\ \rho_2 U \\ \vdots \\ \rho_n U \\ \rho u U + \xi_x p \\ \rho v U + \xi_y p \\ U(e+p) \end{bmatrix}$$

$$\boldsymbol{G} = J^{-1}\begin{bmatrix} \rho_1 V \\ \rho_2 V \\ \vdots \\ \rho_n V \\ \rho u V + \eta_x p \\ \rho v V + \eta_y p \\ V(e+p) \end{bmatrix}, \qquad \boldsymbol{H} = \frac{J^{-1}}{y}\begin{bmatrix} \rho_1 v \\ \rho_2 v \\ \vdots \\ \rho_n v \\ \rho u v \\ \rho v^2 \\ v(e+p) \end{bmatrix} \tag{2}$$

$$\boldsymbol{F}_v = \frac{J^{-1}}{Re}\begin{bmatrix} -\rho_1 U_1^d \\ -\rho_2 U_2^d \\ \vdots \\ -\rho_n U_n^d \\ \xi_x \tau_{xx} + \xi_y \tau_{xy} \\ \xi_x \tau_{xy} + \xi_y \tau_{yy} \\ \xi_x \beta_x + \xi_y \beta_y \end{bmatrix}, \qquad \boldsymbol{H}_v = \frac{J^{-1}}{yRe}\begin{bmatrix} -\rho_1 v_1^d \\ -\rho_2 v_2^d \\ \vdots \\ -\rho_n v_n^d \\ \tau_{xy} \\ \tau_{yy} - \tau_{\theta\theta} \\ \beta_y \end{bmatrix}$$

$$\boldsymbol{G}_v = \frac{J^{-1}}{Re}\begin{bmatrix} -\rho_1 V_1^d \\ -\rho_2 V_2^d \\ \vdots \\ -\rho_n V_n^d \\ \eta_x \tau_{xx} + \eta_y \tau_{xy} \\ \eta_x \tau_{xy} + \eta_y \tau_{yy} \\ \eta_x \beta_x + \eta_y \beta_y \end{bmatrix}, \qquad \boldsymbol{W} = J^{-1}\begin{bmatrix} w_1 \\ w_2 \\ \vdots \\ w_n \\ 0 \\ 0 \\ 0 \end{bmatrix}$$

and

$$\beta_x = u\tau_{xx} + v\tau_{xy} - q_x, \qquad \beta_y = u\tau_{xy} + v\tau_{yy} - q_y \tag{3}$$

The stress tensor components are given by

$$\begin{aligned} \tau_{xx} &= \mu[4/3(\xi_x u_\xi - \eta_x u_\eta) - 2/3(\xi_y v_\xi + \eta_y v_\eta) - j2/3\ v/y] \\ \tau_{yy} &= \mu[4/3(\xi_y v_\xi + \eta_y v_\eta) - 2/3(\xi_x u_\xi + \eta_x u_\eta) - j2/3\ v/y] \\ \tau_{\theta\theta} &= \mu[-2/3(\xi_x u_\xi + \eta_x u_\eta + \xi_y v_\xi + \eta_y v_\eta) + 4/3\ v/y] \\ \tau_{xy} &= \mu(\xi_y u_\xi + \eta_y u_\eta + \xi_x v_\xi + \eta_x u_\eta) \end{aligned} \tag{4}$$

and the heat flux vector components are

$$q_x = -k\frac{\partial T}{\partial x} + \sum_{i=1}^{n} \rho_i u_i^d h_i, \qquad q_y = -k\frac{\partial T}{\partial y} + \sum_{i=1}^{n} \rho_i v_i^d h_i \tag{5}$$

The equations describe two-dimensional flow if $j = 0$ and axisymmetric flow if $j = 1$. The variables are the velocity components u and v, the pressure p, the energy per unit volume e, and the density of the ith species ρ_i, with $\rho = \sum_{i=1}^{n} \rho_i$. The terms w_i represent the production of species from chemical reactions and are calculated by standard methods.[6] The variable y is the cylindrical radius. The grid Jacobian J and the contravariant velocities U and V are defined as follows:

$$\begin{aligned} J^{-1} &= x_\xi y_\eta - x_\eta y_\xi \\ U &= \xi_x u + \xi_y v, \qquad V = \eta_x u + \eta_y v \\ \xi_x &= J y_\eta, \qquad \xi_y = -J x_\eta \\ \eta_x &= -J y_\xi, \qquad \eta_y = J x_\xi \end{aligned} \tag{6}$$

The terms x_ξ, x_η, etc. are the grid metric terms $\partial x/\partial \xi$, $\partial x/\partial \eta$, etc. The contravariant diffusion velocities U_i^d and V_i^d are defined as

$$U_i^d = \xi_x u_i^d + \xi_y v_i^d, \qquad V_i^d = \eta_x u_i^d + \eta_y v_i^d \tag{7}$$

The diffusion velocities are found by Fick's law:

$$\begin{aligned} c_i u_i^d &= -D_i[\xi_x (c_i)_\xi + \eta_x (c_i)_\eta] \\ c_i v_i^d &= -D_i[\xi_y (c_i)_\xi + \eta_y (c_i)_\eta] \end{aligned} \tag{8}$$

where $c_i = \rho_i/\rho$. The mixture viscosity and thermal conductivity, as well as the binary diffusivity of species i in the gas mixture, are expressed as

$$\begin{aligned} \mu &= \mu^{\text{laminar}} + \mu^{\text{turbulent}} \\ k &= k^{\text{laminar}} + k^{\text{turbulent}} \\ D_i &= D_i^{\text{laminar}} + D_i^{\text{turbulent}} \end{aligned} \tag{9}$$

The evaluation of the transport properties in Eq. (9) is discussed in the following. The equation of state used is that for a mixture of thermally perfect gases:

$$p = \sum_{i=1}^{n} \frac{\rho_i}{M_i} RT \tag{10}$$

where M_i is the molecular weight of the ith species, and R is the universal gas constant. The temperature T is determined from the definition of the total energy:

$$\sum_{i=1}^{n} c_i \int^{T} c_{v_i}\, \mathrm{d}T = \frac{e}{\rho} - \frac{1}{2}(u^2 + v^2) - \sum_{i=1}^{n} c_i h_i^0 \tag{11}$$

where c_{v_i} is the specific heat at constant volume of the ith species, and h_i^0 is the heat of formation for species i.

Thermodynamics and Transport Properties

The specific heat, thermal conductivity, and viscosity for each species are determined by fourth-order polynomials of temperature. The coefficients of these polynomials are supplied by McBride and Shuen[13] and are valid up to a temperature of 6000 K. The thermal conductivity and viscosity of the mixture are calculated using Wilke's mixing rule.[14] The binary mass diffusivity D_{ij} between species i and j is obtained using the Chapman-Enskog theory in conjunction with the Lennard-Jones intermolecular potential functions.[14] Then the laminar binary diffusivity of species i in the gas mixture is obtained from

$$D_i^{\text{laminar}} = (1 - X_i) / \sum_{j \neq i}^{n} (X_i / D_{ij}) \tag{12}$$

where X_i is the molar fraction of species i.

Combustion and Turbulence Model

In the present study a seven-species, eight-step reaction mechanism for hydrogen-oxygen combustion is adopted. This model is a reduced reaction mechanism obtained from more complete models by the exclusion of the reactions involving H_2O_2 and HO_2, which could be important in low-temperature ignition studies. A complete description of the reduced model can be found in Ref. 6, together with a discussion of its accuracy and range of application. Further evidence supporting the validity of this combustion model has recently been presented by Sekar et al.[15] In their study of chemically reacting mixing layers, Sekar and co-workers compared the performance of various combustion models. In particular, they found that the results obtained with a 7-species, 7-step reaction mechanism, very similar to the one used in the present study, were nearly identical to those obtained with a more complete 9-species, 18-step model at various inflow conditions.

The turbulent model adopted in the present study is the Baldwin-Lomax algebraic eddy viscosity model[16] and assumes constant turbulent Prandtl and Schmidt numbers ($Pr_t = Sc_t = 0.9$). This model is chosen for its simplicity and computational efficiency.

The interactions between turbulence and chemistry, which enter into the numerical formulation through the source term w_i, represent a very difficult problem. Accounting for such interaction effects would require a closure method such as the probability density function approach or a direct numerical simulation. Since these methods are not yet applicable to complex flows, the interactions between turbulence and chemistry are not considered in the present study.

Numerical Method

The fully coupled Navier-Stokes equations and species continuity equations [Eq. (1)] are solved using a new fully implicit finite difference CFD code. The code employs an iterative method that is based on the LU-SSOR implicit factorization scheme and a second-order symmetric TVD differencing scheme. The iterative scheme can also be combined with the RRE or MPE vector extrapolation techniques to enhance its convergence. A description of the iterative scheme and of one of the extrapolation methods, namely RRE, is given in the following.

Iterative Scheme

Let $\boldsymbol{A}$ and $\boldsymbol{B}$ be the Jacobian matrices of the convective flux vectors, $\boldsymbol{C}$ be the Jacobian of the chemical source term, D_ξ and D_η be difference operators that approximate $\partial/\partial\xi$ and $\partial/\partial\eta$, and $\Delta\boldsymbol{Q}$ be the correction. Then the linearized implicit scheme for Eq. (1), factorized using the LU-SSOR method, can be written as[17,18]

$$\boldsymbol{L}\boldsymbol{T}^{-1}\boldsymbol{U}\Delta\boldsymbol{Q} = -\Delta t[\mathrm{RHS}] \tag{13}$$

where $\boldsymbol{L}$, $\boldsymbol{U}$, and $\boldsymbol{T}$ are the following operators:

$$\boldsymbol{L} = \boldsymbol{I} + \Delta t[D_\xi^- \boldsymbol{A}^+ + D_\eta^- \boldsymbol{B}^+ - \boldsymbol{A}^- - \boldsymbol{B}^- - \boldsymbol{C}] \tag{14}$$

$$\boldsymbol{U} = \boldsymbol{I} + \Delta t[D_\xi^+ \boldsymbol{A}^- + D_\eta^+ \boldsymbol{B}^- + \boldsymbol{A}^+ + \boldsymbol{B}^+] \tag{15}$$

$$\boldsymbol{T} = \boldsymbol{I} + \Delta t[\boldsymbol{A}^+ + \boldsymbol{B}^+ - \boldsymbol{A}^- - \boldsymbol{B}^-] \tag{16}$$

and RHS is the right-hand side residual:

$$\mathrm{RHS} = D_\xi(\boldsymbol{F} - \boldsymbol{F}_v) + D_\eta(\boldsymbol{G} - \boldsymbol{G}_v) + j(\boldsymbol{H} - \boldsymbol{H}_v) - \boldsymbol{W} \tag{17}$$

Here, D_ξ^- and D_η^- are backward difference operators, and D_ξ^+ and D_η^+ are forward difference operators; $\boldsymbol{A}^+$, $\boldsymbol{A}^-$, $\boldsymbol{B}^+$, and $\boldsymbol{B}^-$ are approximately constructed so that the eigenvalues of + matrices are nonnegative and those of − matrices are nonpositive:

$$\boldsymbol{A}^\pm = \tfrac{1}{2}[\boldsymbol{A} \pm \Lambda(\boldsymbol{A})\boldsymbol{I}], \qquad \boldsymbol{B}^\pm = \tfrac{1}{2}[\boldsymbol{B} \pm \Lambda(\boldsymbol{B})\boldsymbol{I}] \tag{18}$$

and

$$\Lambda(\boldsymbol{X}) = \kappa[\max(|\lambda(\boldsymbol{X})|)], \qquad \kappa \geq 1 \tag{19}$$

where $\lambda(\boldsymbol{X})$ represents the eigenvalues of the matrix $\boldsymbol{X}$.

The RHS in Eq. (13) is evaluated as follows. For the viscous flux vectors, central difference operators are used. For the convective flux vectors, D_ξ and D_η are evaluated using the modified flux approach of Harten[19] and Yee[20] to obtain a second-order symmetric TVD scheme:

$$D_\xi \boldsymbol{F} = \frac{\tilde{\boldsymbol{F}}_{j+\frac{1}{2},k} - \tilde{\boldsymbol{F}}_{j-\frac{1}{2},k}}{\Delta\xi} \tag{20}$$

The function $\tilde{\boldsymbol{F}}_{j+\frac{1}{2},k}$ is the numerical flux in the ξ direction evaluated at $(j + \frac{1}{2}, k)$:

$$\tilde{\boldsymbol{F}}_{j+\frac{1}{2},k} = \tfrac{1}{2}(\tilde{\boldsymbol{F}}_{j,k} + \tilde{\boldsymbol{F}}_{j+1,k} + \boldsymbol{R}_{j+\frac{1}{2}}\boldsymbol{\Phi}_{j+\frac{1}{2}}) \tag{21}$$

where $\boldsymbol{R}_{j+\frac{1}{2}}$ denotes the matrix of eigenvectors of the flux Jacobian matrix $\boldsymbol{A}$ evaluated at some symmetric average of $\boldsymbol{Q}_{j,k}$ and $\boldsymbol{Q}_{j+1,k}$, denoted as $\boldsymbol{Q}_{j+\frac{1}{2}}$. Similarly, one can define in this manner the numerical flux in the η direction.

The elements $\phi^l_{j+\frac{1}{2}}$ of the dissipation vector $\boldsymbol{\Phi}_{j+\frac{1}{2}}$ are

$$\phi^l_{j+\frac{1}{2}} = -\Psi(a^l_{j+\frac{1}{2}})[\alpha^l_{j+\frac{1}{2}} - \hat{Q}^l_{j+\frac{1}{2}}] \tag{22}$$

$$\boldsymbol{\alpha}_{j+\frac{1}{2}} = \frac{\boldsymbol{R}^{-1}_{j+\frac{1}{2}}(\boldsymbol{Q}_{j+1,k}J_{j+1,k} - \boldsymbol{Q}_{j,k}J_{j,k})}{0.5(J_{j+1,k} + J_{j,k})} \tag{23}$$

where $a^l_{j+\frac{1}{2}}$ denotes the eigenvalues of $\boldsymbol{A}$ evaluated at $\boldsymbol{Q}_{j+\frac{1}{2}}$, and $\alpha^l_{j+\frac{1}{2}}$ denotes the elements of the vector $\boldsymbol{\alpha}_{j+\frac{1}{2}}$. The function Ψ is

$$\Psi(z) = \begin{cases} |z|, & |z| \geq \epsilon \\ \dfrac{(z^2 + \epsilon^2)}{2\epsilon}, & |z| < \epsilon \end{cases} \tag{24}$$

The term ϵ in Eq. (24) is taken to be a function of the velocity and sound speed[21]:

$$\epsilon_{j+\frac{1}{2}} = \tilde{\epsilon}\{\,|U_{j+\frac{1}{2}}| + |V_{j+\frac{1}{2}}| + \tfrac{1}{2}[(\sqrt{\xi_x^2 + \xi_y^2} + \sqrt{\eta_x^2 + \eta_y^2})a]_{j+\frac{1}{2}}\} \tag{25}$$

where a is the frozen sound speed, and $\tilde{\epsilon}$ is a small number in the range $0 \le \tilde{\epsilon} \le 0.4$, which controls the convergence rate and the sharpness of discontinuities. The "limiter" functions $\hat{Q}_{j+1/2}$ used in this study are the following:

$$\hat{Q}^l_{j+1/2} = \text{minmod}(\alpha^l_{j-1/2}, \alpha^l_{j+1/2}, \alpha^l_{j+3/2}) \tag{26}$$

$$\hat{Q}^l_{j+1/2} = \text{minmod}[2\alpha^l_{j-1/2}, 2\alpha^l_{j+1/2}, 2\alpha^l_{j+3/2}, \tfrac{1}{2}(\alpha^l_{j-1/2} + \alpha^l_{j+3/2})] \tag{27}$$

Except where indicated, all of the results presented here were obtained with the limiter given in Eq. (26).

The eigenvalues and eigenvectors of the fully coupled chemically reacting equations, as well as the resulting expressions for $R\Phi$, are given in Ref. 6. This scheme is second-order accurate in space and is suitable for steady-state calculations.

Extrapolation Method for Convergence Acceleration

There are several extrapolation methods for achieving faster convergence rates in the literature. Of these methods, MPE and RRE seem to be the most efficient as far as the amount of computing and storage requirements are concerned. In the present study, both MPE and RRE are used in the so-called cycling mode through their implementations given in the recent work of Sidi and Celestina[22] and Sidi.[23] A brief description of the cycling mode is given in the following. More details and further references concerning these methods and others are given in Refs. 22 and 23.

Step 1. Given an initial approximation Q^0, use the iterative scheme to generate the sequence of approximations Q^1, $Q^2, \ldots, Q^{N_0}$, and set $Q^{N_0} \rightarrow Q^0$ and $q = 1$. Here, N_0 is a given positive integer and q is the number of cycles.

Step 2. Beginning now with Q^0, generate the sequence Q^1, $Q^2, \ldots, Q^{K_{\max}+1}$ for some fixed integer $K_{\max}$.

Step 3. Apply RRE (or MPE) to this sequence to obtain the approximation $S^{q+1} \equiv S_{0,K_{\max}}$. (The determination of $S_{0,K_{\max}}$ from $Q^1, Q^2, \ldots, Q^{K_{\max}+1}$ will be described later.)

Step 4. If S^{q+1} is a satisfactory approximation, stop; otherwise, replace Q^0 by S^{q+1} and q by $q+1$ and go to step 2.

In general, it is observed that the sequence of approximations $S^1, S^2, \ldots$ has better convergence properties than the sequence obtained from the iterative scheme alone. A brief outline of RRE is given below for MPE (see Refs. 22 and 23).

Given the vector sequence $Q^0, Q^1, \ldots, Q^{k+1}$, with $k = K_{\max}$, compute the differences:

$$\Delta Q^j = Q^{j+1} - Q^j, \qquad j = 0, 1, \ldots, k \tag{28}$$

Next, determine the scalars $\gamma_0, \gamma_1, \ldots, \gamma_k$ by solving the constrained least-squares problem,

$$\text{minimize} \left\| \sum_{j=0}^{k} \gamma_j \Delta Q^j \right\| \tag{29}$$

subject to $\sum_{j=0}^{k} \gamma_j = 1$. Finally, set

$$S_{0,K} = \sum_{j=0}^{k} \gamma_j Q^j \tag{30}$$

Although the original definition of RRE is different, the definition given earlier is equivalent to it and results in an implementation that is more stable numerically.

Results

The numerical scheme described earlier has been validated by using benchmark test cases for which experimental or numerical results are available. Two such validation test cases will be presented here, preceding the discussion of shock-wave/boundary-layer interactions in premixed H_2-air hypersonic flows: 1) the two-dimensional shock-wave/boundary-layer interactions in a laminar nonreacting airflow and 2) the combustion of a premixed hydrogen-air supersonic flow over a compression corner.

Benchmark Test Cases

The first test case considers a nonreacting airflow in which an oblique shock impinges on a laminar boundary layer developing on an adiabatic flat plate. The test problem corresponds to the experiments of Hakkinen et al.,[24] who considered a 3-deg shock generator configuration in a $M = 2$ airflow. The Reynolds number based on freestream conditions, and the length from the leading edge of the plate to the shock impingement point is 2.96×10^5. The shock is sufficiently strong to cause a separation of the boundary layer. Several numerical results for this problem have been reported in the literature.[25-27]

The computations were done on three different grids having uniform mesh increments in the horizontal direction (Δx), and an exponentially stretched mesh in the vertical direction (Δy). The horizontal coordinate is set to $x = 0$ at the leading edge and $x = L$ at the shock impingement point. The initial grid contained 30×56 points, for which $\Delta x/L = 0.0625$ and $(\Delta y/L)_{\min} = 7.83 \times 10^{-4}$. The other grids contained two and three times the initial number of grid points in both the x and y directions.

The computational results from the grid refinement study are shown in Fig. 2. The initial grid density is too coarse to adequately resolve the pressure plateau or the skin friction. As shown in Fig. 2, details of the flowfield are generally resolved with the second grid, although a small difference exists between the second and third grids near the shock impingement point. Outside the separated flow region, very small differences exist in the results obtained from the three grids. These results were obtained with the limiter given in Eq. (27).

The computations for each of the three grids were initialized with freestream conditions in the interior of the domain. On the coarse grid, the L_2 norm of the density residual was reduced four orders of magnitude in 900 iterations. On the other two grids the same reduction was achieved in 1400 and 1900 iterations, respectively.

A comparison of the present results with experiment and other numerical calculations is shown in Fig. 3. All of the

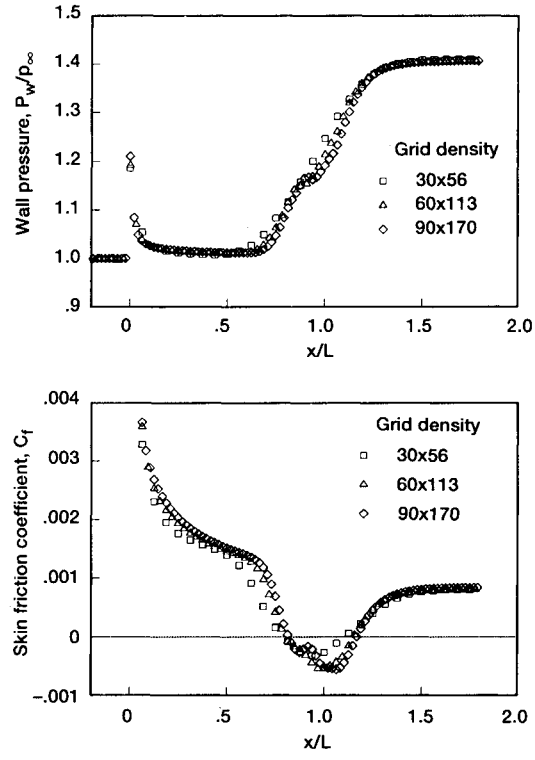

Fig. 2 Grid refinement for nonreacting shock-wave/boundary-layer interaction ($M = 2$, $Re_L = 2.96 \times 10^5$).

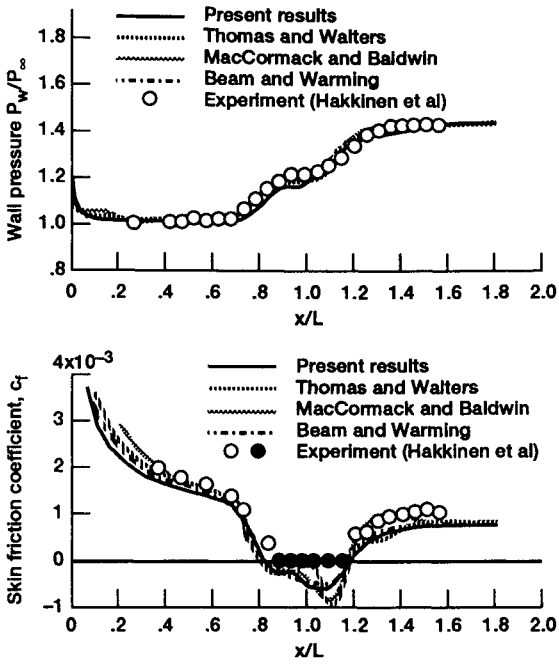

Fig. 3 Comparison of computational and experimental results for nonreacting shock-wave/boundary-layer interaction.

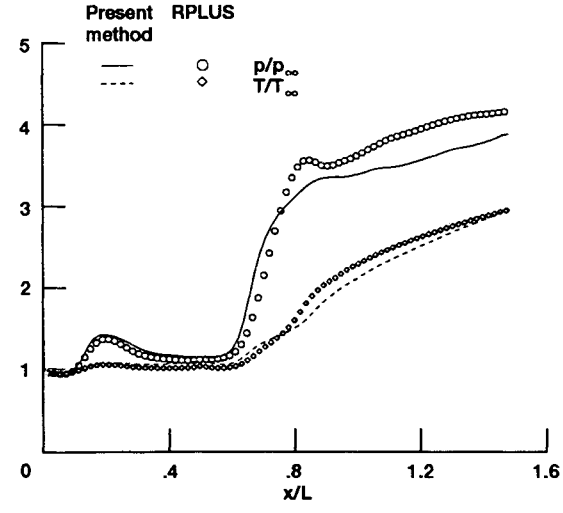

Fig. 4 Pressure and temperature variation along gridline located 0.2 cm from base of ramp ($M = 4.5$, $T_\infty = 900$ K, $p_\infty = 1$ atm).

results were obtained with the complete Navier-Stokes equations, except for the computations of Thomas and Walters,[27] which were performed with the thin-layer assumption. The agreement between all of the computations and the experiment is generally good, although noticeable differences exist in the predicted skin-friction level in the separated zone. No experimental values of the skin friction were reported in the separated zone. The solid symbols in Fig. 3 indicate the observed separated region.

The second test problem considered in the present paper is the combustion of a premixed stoichiometric hydrogen-air supersonic flow ($M = 4.5$) over a 10-deg compression ramp. The inflow conditions are $T_\infty = 900$ K and $p_\infty = 1$ atm. The shock wave is strong enough to ignite the mixture, and a shock-deflagration wave is established. The computations were conducted using the present method and the RPLUS code developed by Shuen and Yoon[18] on a 80 × 51 grid corresponding to that described in Ref. 18. A fully turbulent flow and an adiabatic, noncatalytic wall boundary condition were assumed. The RPLUS version of the code used in this study employs a centered differenced scheme with artificial dissipation and a 9-species, 18-step combustion model.[18]

Figure 4 shows a comparison of the pressure and temperature variation along the grid line located 0.2 cm from the base of the ramp. Here, L is a characteristic length and was set to $L = 2$ cm in the present case. The results obtained with the two codes are in reasonably good agreement, showing a maximum difference of ~ 10% in the pressure distribution. The small differences observed in Fig. 4 can mainly be attributed to the different combustion models and differencing schemes used in the two codes.

Figure 5 compares the convergence histories obtained using the present basic iterative scheme alone and after it is combined with RRE and MPE in the cycling mode with $K_{max} = 10$ and after 200 initial iterations. It can be seen that RRE converges slightly faster than MPE. A reduction of approximately five orders of magnitude is achieved without extrapolation in 1000 iterations, whereas with RRE and MPE this takes only 620 and 670 iterations, respectively. The overhead in CPU time due to the use of extrapolation turned out to be very small (< 1%), and the only disadvantage associated with these extrapolation techniques is the need to store K_{max} additional vectors.

Shock-Wave/Boundary-Layer Interactions in Premixed H_2-Air Hypersonic Flow

The interaction between a shock wave and a boundary layer in premixed combustible gases is investigated on an axisymmetric ram accelerator configuration having dimensions similar to those of the experimental device presently operating at the University of Washington.[3-9] The configuration geometry is shown in Fig. 1, and only the frontal part of the projectile ($0 \le x/L \le 0.61$) is considered initially. A stoichiometric H_2-air mixture at a temperature and pressure of $T_\infty = 300$ K and $p_\infty = 1$ atm is considered. A constant projectile surface temperature $T_w = 600$ K is assumed in all of the calculations, and the flow is also assumed to be fully turbulent along the entire projectile.

Computations were conducted for a projectile moving at a Mach number $M = 6.7$, for which it was assumed first that no chemical reactions occur (the chemistry part was switched "off"). The corresponding Reynolds number per unit length at these conditions was 1.21×10^8/m. Figure 6 shows nondimensional temperature (T/T_∞) and Mach number contours obtained on a 165 × 75 grid. For clarity, the plot is magnified in the vertical direction by a factor of two. Note the high temperature that is created in the boundary layer immediately behind the shock impingement point. When the chemical reactions are switched "on," combustion will start in this region.

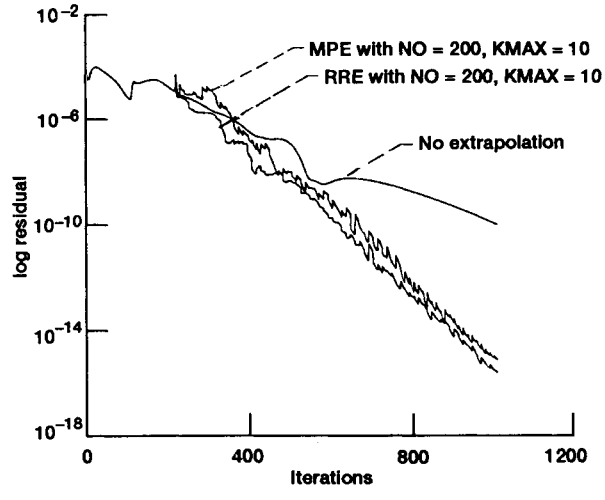

Fig. 5 Convergence history of L_2 density residual for reacting flow past a compression corner. Grid is 80 × 50.

This is shown in Fig. 7, where nondimensional temperature contours are plotted near the shock impingement point after 100 iterations, starting from the nonreacting solution. There is clearly an induction zone followed by a heat release zone in which the temperature increases sharply. The flame then propagates outward and upstream (through the boundary layer) and eventually couples with the reflected shock, establishing a shock-deflagration wave. The stable, converged solution is shown in Fig. 8 in the form of nondimensional temperature and Mach number contours. The combustion process causes the shock reflected from the projectile surface to bend upward. The reason for this rotation of the wave has been pointed out by Cambier et al.[28] and is explained as follows. The heat from combustion accelerates the flow in a direction normal to the shock wave. Since the flow deflection remains the same for a fixed geometry, and since the tangential component of the velocity remains the same across the shock, there must be an increase of the wave angle toward a normal wave.

Computational results from a grid refinement study are shown in Fig. 9, where the skin friction coefficient and surface pressure are plotted in the interaction region for the baseline grid (165 × 75), and for coarser (125 × 50), and finer (195 × 90) grids. A nonuniform horizontal spacing, $\Delta x/L$, of 0.0038, 0.0021, and 0.0016 was used for the coarse, nominal, and fine grids, respectively. Exponentially stretched increments in the vertical direction were used for all of the grids, with a minimum value of y^+ at points nearest to the wall equal to 3.0, 2.0, and 1.5 for the three grids, respectively. The (125 × 50) grid is too coarse to adequately resolve the boundary layer. As shown in Fig. 9, details of the interaction are generally resolved with the baseline grid, although the pressure peak is slightly under-

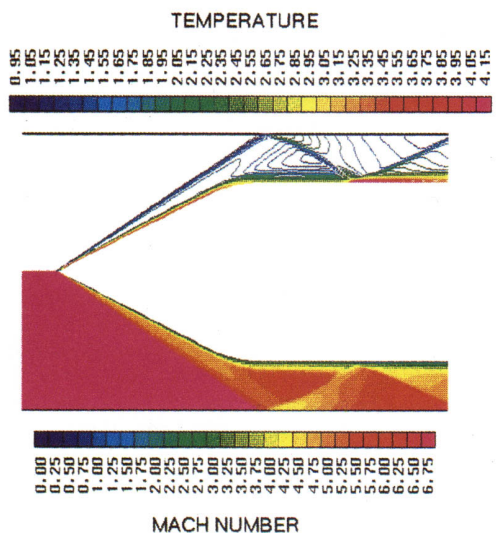

Fig. 6 Nondimensional temperature T/T_∞ (top) and Mach number (bottom) contours for nonreacting $M = 6.7$ flow. For clarity, the vertical direction is magnified by a factor of two.

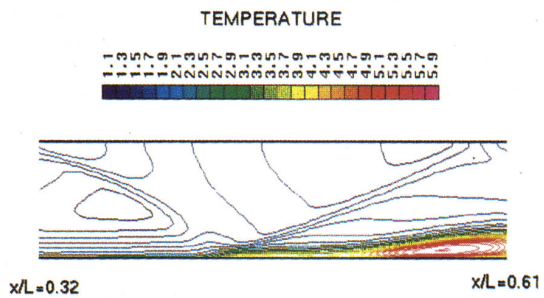

Fig. 7 Detail of reacting shock-wave/boundary-layer interaction after 100 iterations ($M = 6.7$).

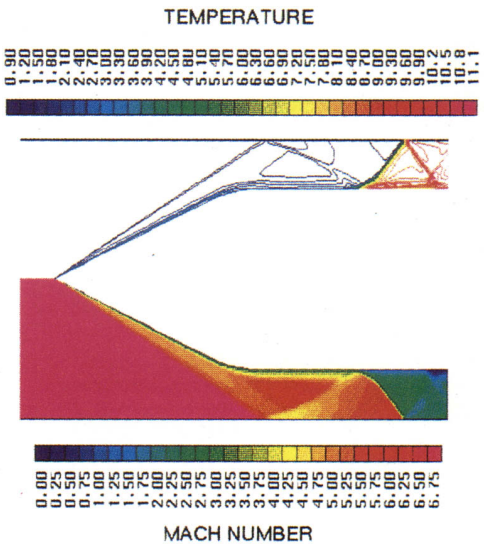

Fig. 8 Nondimensional temperature T/T_∞ (top) and Mach number (bottom) contours showing converged solution for reacting $M = 6.7$ flow.

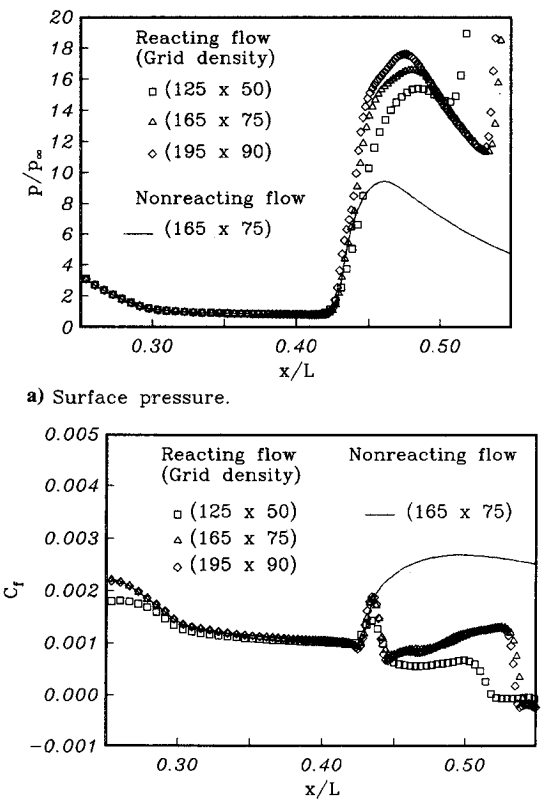

Fig. 9 Grid refinement for reacting shock-wave/boundary-layer interaction in a ram accelerator configuration.

predicted. Ahead of the interaction, all three grids give nearly identical surface pressure and skin friction distributions. In general, the reacting flow solutions show a greater grid sensitivity than the nonreacting case. This result is due to the stiffness and the strong nonlinear behavior introduced by the chemical source term.

For comparison, the nonreacting solution on the nominal grid is also plotted in Fig. 9. In the nonreacting flow case, the skin-friction coefficient increases across the interaction region. This increase is typical of high Mach number flows and

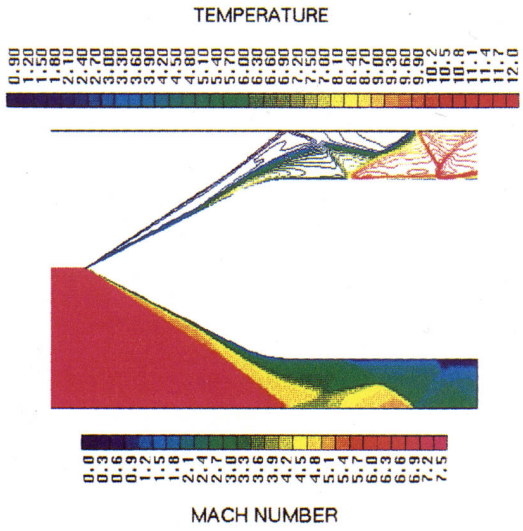

Fig. 10 Nondimensional temperature T/T_∞ (top) and Mach number (bottom) contours showing converged solution for reacting $M = 7.1$ flow.

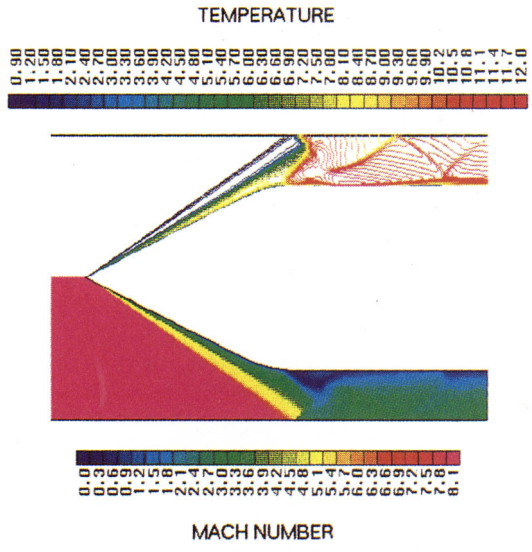

Fig. 11 Nondimensional temperature T/T_∞ (top) and Mach number (bottom) contours showing converged solution for reacting $M = 8.0$ flow.

can be explained as follows. The shear stress τ in the wall layer is given by

$$-\rho\overline{u'v'} + \frac{\mu}{Re}\frac{\partial u}{\partial n} = \tau \tag{31}$$

Assuming that the pressure gradient and inertia terms give higher-order corrections even in the interaction region, it can be shown[29] that the shear stress is constant across the wall layer (constant stress layer); therefore,

$$\tau_w = \tau = -\rho\overline{u'v'} + \frac{\mu}{Re}\frac{\partial u}{\partial n} \tag{32}$$

where τ_w is the wall shear stress. Consider then a streamline somewhat outside the viscous sublayer where the viscous stress becomes small compared to the Reynolds stress. Along this streamline, as the flow is decelerated across the shock, $\overline{u'v'}$ decreases, but the density ρ increases. At high Mach numbers, the jump in density across the shock wave is large and the Reynolds stress increases.

When combustion takes place behind the interaction, the density increases first across the shock but decreases immediately behind it due to the combustion process, which produces a high-temperature/low-density boundary layer. The result is a "spike" shown in Fig. 9b and a reduction in the skin-friction coefficient downstream. The combustion process also substantially increases the pressure levels on the projectile, and makes the boundary layer more susceptible to separation.

For a higher Mach number flow ($M = 7.1$), combustion begins prematurely in the boundary layer, at a location just upstream of the projectile shoulder, as shown in Fig. 10. Note again the curving of the nose shock due to the combustion in the boundary layer. A very complex interaction between the shock-wave system and the chemically reacting boundary layer is observed downstream. Complete combustion is achieved behind the shock being reflected from the projectile surface. At a still higher Mach number, $M = 8$, combustion takes place along the entire boundary layer at the nose of the projectile, as shown in Fig. 11. Complete combustion is achieved in this case behind the first reflected shock wave from the tube wall, which also creates a large separation bubble on the projectile surface. The results shown in Figs. 10 and 11 were obtained on the nominal grid.

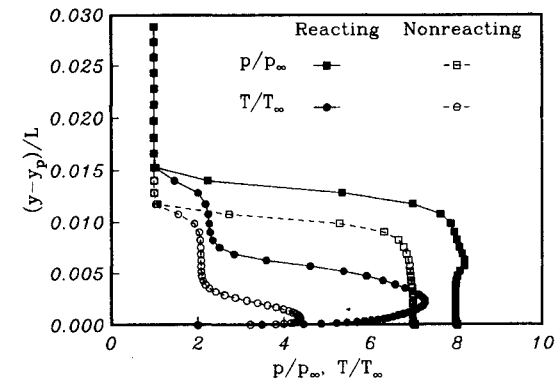

a) Pressure and Temperature.

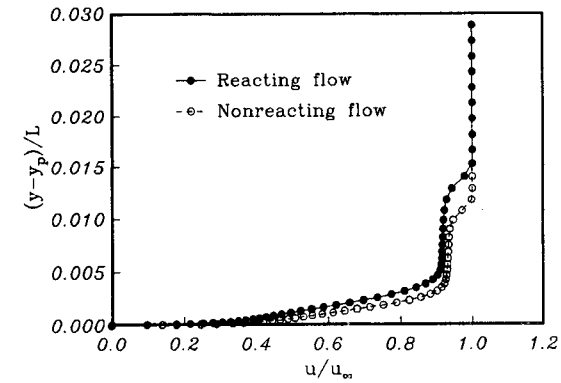

b) Streamwise velocity.

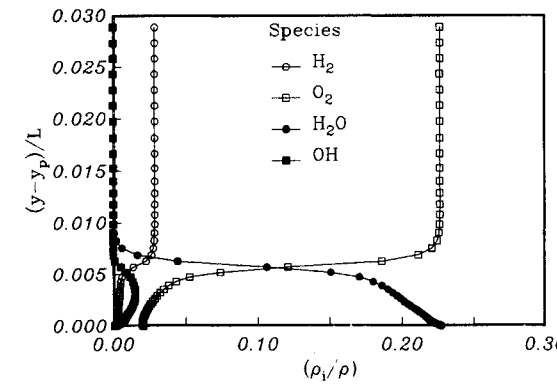

c) Species mass fraction.

Fig. 12 Distribution of physical quantities in the boundary layer at station $x/L = 0.14$.

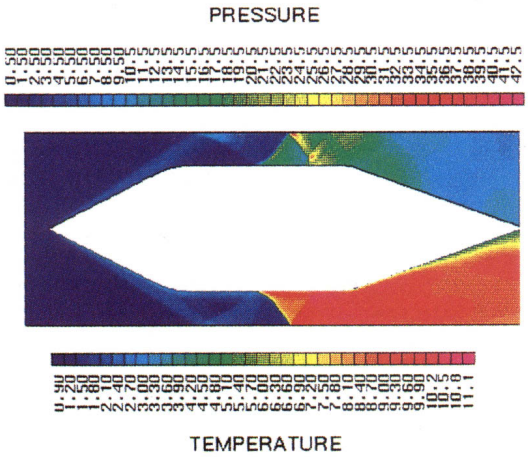

Fig. 13 Nondimensional pressure p/p_∞ (top) and temperature T/T_∞ (bottom) contours showing converged solution for a complete ram accelerator configuration ($M = 6.7$).

The temperature, pressure, velocity, and major species concentration in the boundary layer, at the station $x/L = 0.14$ (corresponding approximately to the midpoint of the nose cone), are shown in Fig. 12. After the radial coordinate of the projectile surface is denoted by y_p, the flow variables are plotted as a function of the nondimensional radial distance from the projectile surface. Figure 12a compares the pressure and temperature profiles in the boundary layer for reacting and nonreacting flow. The wall temperature was assumed to be 600 K; thus, both temperature curves start at $T/T_\infty = 2$ on the surface. Away from the surface, the temperature in the chemically reacting boundary layer reaches a maximum value of $T_{\max} \approx 2200$ K, compared to $T_{\max} \approx 1320$ K for the nonreacting flow. The flame propagating away from the surface noticeably expands the thermal boundary layer. Associated with this flame is also the very small pressure drop seen close to the surface in the reacting pressure curve. The combustion process also produces a shock with a higher inclination angle. As a result, the postshock temperature and pressure for the reacting flow are higher and the postshock velocity is lower (Fig. 12b). The effect of combustion on the velocity profile in the boundary layer is much smaller than that on temperature or pressure.

The mass fraction profiles of the major species in the boundary layer are shown in Fig. 12c. Since a cold wall is assumed, there is a marked decrease in the amount of OH near the surface and a corresponding increase in the amount of H_2O. All other species not plotted are present in much smaller concentrations.

Finally, the results obtained for a complete ram accelerator projectile (using an extended nominal grid of 245×75) are shown in Fig. 13. The inflow conditions are the same as those in Fig. 8. Note that the combustion process occurring behind the reflected shock wave from the projectile surface produces a high pressure region over the back of the projectile resulting in a net positive thrust force. Defining A_t as the tube cross-sectional area and F as the net thrust force on the projectile (including the effects of the viscous drag), a net nondimensional thrust force of magnitude $\tilde{F} = F/p_\infty A_t = 3.10$ was obtained at the present conditions. The viscous drag reduced the thrust on the projectile by $\sim 10\%$.

Conclusions

A new CFD code, based on the LU-SSOR implicit factorization scheme and a second-order TVD differencing scheme, has been developed for solving the fully coupled two-dimensional/axisymmetric Reynolds-averaged Navier-Stokes equations and species continuity equations in an efficient manner. Vector extrapolation methods used in combination with the basic iterative scheme significantly improved the convergence rate and resulted in a very small overhead in CPU time. The code has been used to study shock-wave/boundary-layer interactions in a ram accelerator configuration. Results indicate a combustion mechanism in which a shock wave induces combustion in the boundary layer, which then couples with the reflected shock, forming a shock-deflagration wave. At higher Mach numbers, spontaneous ignition in part of the boundary layer was observed, which eventually extended along the entire boundary layer at still higher values of the Mach number.

The present results indicate that viscous effects are of primary importance in a ram accelerator configuration. For the cases considered, combustion always started in the boundary layer and strongly affected the entire flowfield.

Acknowledgments

This work was supported by the Numerical Aerodynamic Simulation Program (NAS). The author thanks Jian-Shun Shuen of the NASA Lewis Research Center for his help during the development of the computer code. Thanks are also due to Avram Sidi of the Technion-Israel Institute of Technology for his guidance during the implementation of his vector extrapolation code.

References

[1]Adamson, T. C., and Messiter, A. F., "Analysis of Two-Dimensional Interactions Between Shock Waves and Boundary Layers," *Annual Review of Fluid Mechanics,* Vol. 12, 1980, pp. 103–138.

[2]Delery, J., and Marvin, J. G., "Shock-Wave Boundary Layer Interactions," AGARD-AG-280, Feb. 1986.

[3]Hertzberg, A., Bruckner, A. P., and Bogdanoff, D. W., "Ram Accelerator: A New Chemical Method for Accelerating Projectiles to Ultrahigh Velocities," *AIAA Journal,* Vol. 26, No. 2, 1988, pp. 195–203.

[4]Bruckner, A. P., Knowlen, C., Hertzberg, A., and Bogdanoff, D. W., "Operational Characteristics of the Thermally Choked Ram Accelerator," *Journal of Propulsion and Power,* Vol. 7, No. 5, 1991, pp. 828–836.

[5]Brackett, D. C., and Bogdanoff, D. W., "Computational Investigation of Oblique Detonation Ramjet-in-Tube Concepts," *Journal of Propulsion and Power,* Vol. 5, No. 3, May 1989, pp. 276–281.

[6]Yungster, S., Eberhardt, S., and Bruckner, A. P., "Numerical Simulation of Hypervelocity Projectiles in Detonable Gases," *AIAA Journal,* Vol. 29, No. 2, 1991, pp. 187–199.

[7]Yungster, S., and Bruckner, A. P., "Computational Studies of a Superdetonative Ram Accelerator Mode," *Journal of Propulsion and Power,* Vol. 8, No. 2, 1992, pp. 457–463.

[8]Kull, A., Burnham, E., Knowlen, C., Hertzberg, A., and Bruckner, A. P., "Experimental Studies of Superdetonative Ram Accelerator Modes," AIAA Paper 89-2632, July 1989.

[9]Bruckner, A. P., and Hertzberg, A., "Ram Accelerator Direct Launch System for Space Cargo," International Astronautical Federation Paper IAF-87-211, 38th Congress of the International Astronautical Federation, Brighton, England, Oct. 1987.

[10]Humphrey, J. W., "Parametric Study of an ODW Scramaccelerator for Hypersonic Test Facilities," AIAA Paper 90-2470, July 1990.

[11]Rom, J., and Kivity, Y., "Accelerating Projectiles up to 12 km/s Utilizing the Continuous Detonation Propulsion Method," AIAA Paper 88-2969, July 1988.

[12]Yip, G. T., Strawa, A. W., and Chapman, G. T., "Streamtube Analysis of Supersonic Combustion in an In-Tube-Scramjet," AIAA Paper 90-2339, July 1990.

[13]McBride, B. J., and Shuen, J. S., private communication, NASA Lewis Research Center, Cleveland, OH, Jan. 1990.

[14]Anderson, J. D., *Hypersonic and High Temperature Gas Dynamics,* McGraw-Hill, New York, 1989, pp. 596–600.

[15]Sekar, B., Mukunda, H. S., and Carpenter, M. H., "The Direct Simulation of High-Speed Mixing-Layers Without and With Chemical Heat Release," *Computational Fluid Dynamics Symposium on Aeropropulsion,* NASA CP-10045, Cleveland, OH, April 1990.

[16]Baldwin, B., and Lomax, H., "Thin Layer Approximation and Algebraic Model for Separated Turbulent Flows," AIAA Paper 78-257, Jan. 1978.

[17]Jameson, A., and Yoon, S., "Lower-Upper Implicit Schemes with Multiple Grids for the Euler Equations," *AIAA Journal,* Vol. 25, No. 7, 1987, pp. 929–935.

[18]Shuen, J. S., and Yoon, S., "Numerical Study of Chemically Reacting Flows Using a Lower-Upper Symmetric Successive Overre-

laxation Scheme," *AIAA Journal,* Vol. 27, No. 12, 1989, pp. 1752–1760.

[19]Harten, A., "On a Class of High Resolution Total-Variation-Stable Finite Difference Schemes," *SIAM Journal of Numerical Analysis,* Vol. 21, No. 1, 1984, pp. 1–23.

[20]Yee, H. C., "Upwind and Symmetric Shock-Capturing Schemes," NASA TM-89464, May 1987.

[21]Yee, H. C., Klopfer, G. H., and Montagnè, J.-L., "High-Resolution Shock-Capturing Schemes for Inviscid and Viscous Hypersonic Flows," NASA TM-100097, April 1988.

[22]Sidi, A., and Celestina, M. L., "Convergence Acceleration for Vector Sequences and Applications to Computational Fluid Dynamics," NASA TM-101327, ICOMP-88-17, Aug. 1988.

[23]Sidi, A., "Efficient Implementation of Minimal Polynomial and Reduced Rank Extrapolation Methods," NASA TM-103240, ICOMP-90-20, Aug. 1990.

[24]Hakkinen, R. J., Greber, I., Trilling, L., and Abarbanel, S. S., "The Interaction of an Oblique Shock Wave with a Laminar Boundary Layer," NASA Memo-2-18-59W, March 1959.

[25]MacCormack, R. W., and Baldwin, B. S., "A Numerical Method for Solving the Navier-Stokes Equations with Application to Shock-Boundary Layer Interactions," AIAA Paper 75-1, Jan. 1975.

[26]Beam, R. M., and Warming, R. F., "An Implicit Factored Scheme for the Compressible Navier-Stokes Equations," *AIAA Journal,* Vol. 16, No. 4, 1978, pp. 393–402.

[27]Thomas, L. T., and Walters, R. W., "Upwind Relaxation Algorithms for the Navier-Stokes Equations," *AIAA Journal,* Vol. 25, No. 4, 1987, pp. 527–534.

[28]Cambier, J. L., Adelman, H., and Menees, G. P., "Numerical Simulations of Oblique Detonations in Supersonic Combustion Chambers," *Journal of Propulsion and Power,* Vol. 5, No. 4, July 1989, pp. 482–491.

[29]Tennekes, H., and Lumley, J. L., *A First Course in Turbulence,* MIT Press, Cambridge, MA, 1972, pp. 182–186.